Influence of interlayer stacking on optical behavior in WSe_2/MoS_2 van der Waals heterostructures

Widad Louafi,[1,*] Karim Rezouali,[1,2,3] Daniele Varsano,[4,5] Maurizia Palummo,[4,5,6] Maurits W. Haverkort,[7] and Samir Lounis[3,8]

[1]*Laboratoire de Physique Théorique, Faculté des Sciences Exactes, Université de Bejaia, 06000 Bejaia, Algérie*
[2]*Faculty of Physics and CENIDE, University of Duisburg-Essen, D-47053 Duisburg, Germany*
[3]*Peter Grünberg Institut, Forschungszentrum Jülich and JARA, D-52425 Jülich, Germany*
[4]*Centro S3, Istituto Nanoscienze—Consiglio Nazionale delle Ricerche (CNR-NANO), via Campi 213/A, 41125 Modena, Italy*
[5]*European Theoretical Spectroscopy Facility (ETSF)*
[6]*Dipartimento di Fisica, Università di Roma 'Tor Vergata,' Via della Ricerca Scientifica 1, I-00133 Roma, Italy*
[7]*Institute for Theoretical Physics, Heidelberg University, 69120 Heidelberg, Germany*
[8]*Institute of Physics, Martin-Luther-University Halle-Wittenberg, 06099 Halle (Saale), Germany*

(Received 20 June 2025; revised 23 September 2025; accepted 24 October 2025; published 12 November 2025)

We investigate the impact of crystal alignment on excitonic behavior in WSe_2/MoS_2 van der Waals heterostructures by comparing eclipsed (AA) and staggered (AB) stacking configurations. Our first-principles and symmetry-based analysis reveal that interlayer stacking symmetry plays a central role in determining the nature of electron-hole pairs. We uncover a rich variety of excitonic states, including spatially confined two-dimensional (2D) excitons, delocalized three-dimensional (3D) excitons, and charge-transfer (CT) excitons with interlayer character. The dimensionality and optical activity of these excitons are governed by the interplay among orbital character, interlayer hybridization, and symmetry-imposed selection rules. Our findings establish general principles for engineering excitonic properties in van der Waals heterostructures through controlled layer orientation and stacking order.

DOI: 10.1103/n6py-mmq7

I. INTRODUCTION

Two-dimensional (2D) semiconducting materials made of transition metal dichalcogenides (TMDs) have recently gained popularity due to their intriguing physical and chemical properties, which hold promise for the next generation of optoelectronic, photonic, and energy conversion devices [1–6].

Among others, monolayers WSe_2 and MoS_2 are two important members of these materials, composed of a hexagonal sheet of transition metal atoms (Mo, W) sandwiched between two sheets of chalcogen atoms (S, Se), which are held together by covalent bonds. The category of these two 2D materials fabricated by means of mechanical exfoliation, are finite band gap materials exhibiting direct fundamental gaps spanning the visible to near-infrared (NIR) spectrum. This characteristic enables efficient light-matter interaction [7] and opens a large avenue for applications in photodetectors [8,9], light-emitting diodes (LEDs) [10–12], and photovoltaic devices [13,14]. The strong excitonic effects observed in these materials further enhance their optical performance, making them ideal candidates for nanoscale optoelectronic devices [15].

A critical trait of TMD monolayers is that their electronic and optical properties are valley-dependent, a consequence of strong spin-orbit coupling and broken inversion symmetry [16,17]. The development of valleytronics, an emerging discipline that exploits the degree of freedom of valleys for information processing and storage [18–20], is made possible by the presence of distinct valleys at the K and K' points of the Brillouin zone (BZ).

The electronic properties of TMD monolayers can be engineered by creating heterostructures through stacking different monolayers. These heterostructures are kept together by weak van der Waals (vdW) forces, allowing for precise control over layer composition, stacking orientation, and interlayer coupling [1,21,22]. A particularly intriguing configuration is the type-II band alignment, where the conduction band minimum (CB) of one material aligns with the valence band maximum (VB) of the adjacent layer. This staggered energy level arrangement enables the spatial separation of photoexcited charge carriers, making type-II heterojunctions worth using in photovoltaics, photodetectors, and photocatalysis [23,24].

TMD heterostructures also exhibit efficient exciton dissociation and charge transfer processes, which are crucial to the performance of optoelectronic devices. These structures exploit the tunability of interlayer excitons, in which electrons and holes reside in distinct layers, resulting in prolonged excitonic radiative lifetime and consequently higher device efficiency [25,26]. For instance, WSe_2/MoS_2 and $WS_2/MoSe_2$ heterostructures have shown extraordinary performance in charge carrier separation and energy conversion applications [14,27]. Due to the presence of type-II band alignment and tailored vdW interactions, these systems were able to produce photocurrent and harvest energy more effectively [28,29].

*Contact author: widad.louafi@univ-bejaia.dz

Going beyond optoelectronic applications, TMD heterostructures are emerging as promising platforms for quantum technologies. Twisting adjacent TMD layers to form Moiré superlattices enables the emergence of flat electronic bands, which host correlated phenomena such as Mott insulating states and superconductivity [30,31]. The Moiré potential landscape that results offers a highly tunable platform for the investigation of strong electronic correlations and quantum phase transitions, thereby emphasizing their potential to advance both fundamental quantum science and device engineering. Moreover, the integration of TMD heterostructures with other 2D materials, such as graphene and hexagonal boron nitride (hBN), broadens their portfolios for device layouts. Graphene, with its high electrical conductivity and flexibility, functions as an ideal electrode material, while hBN provides an atomically smooth insulating layer with minimal charge traps [32]. These hybrid systems enabled the building of innovative devices, such as tunneling transistors, vertical heterojunction diodes, and flexible electronics [33].

In this work, we investigate the optoelectronic properties of WSe_2/MoS_2 bilayer vdW periodic heterojunctions, focusing on the three stackings that correspond to local energy minima in R-type Moiré patterns [22]. Here, the term R-type Moiré pattern refers to a rotation-type Moiré, which arises when two periodic lattices are stacked with a small relative rotation. This produces a larger-scale interference pattern, known as the Moiré superlattice, whose periodicity depends on the rotation angle. Using a highly precise, state-of-the-art ab initio many-body approach, we analyze the spectra in detail and demonstrate that the nature and dimensionality of excitons in these heterojunctions can be systematically controlled. Our findings reveal the significant impact of stacking configurations on the optical excitations at the absorption onset. By systematically varying the arrangement of the WSe_2 and MoS_2 layers, we identify three distinct types of electron-hole pairs of two-dimensional (2D) intralayer excitons, three-dimensional (3D) interlayer excitons, and charge-transfer (CT) excitons. We further discuss their emergence based on symmetry considerations, providing a deeper understanding of the relationship between stacking order and excitonic properties in vdW heterostructures.

The paper is organized as follows. Section II describes the computational methods employed in this study. Section III presents and discusses our results, and Sec. IV summarizes the main conclusions.

II. METHOD

We performed density functional theory (DFT) [34,35], *GW* [36–39], and Bethe–Salpeter equation (BSE) formalism [38–41] utilizing the Quantum Espresso [42] and Yambo [43,44] codes. This allows for a sufficiently accurate description of both the ground-state (DFT), one-particle excitation energies (*GW*), and two-particle excitonic excitations as observed in optical experiments (BSE).

We first calculated the ground-state properties utilizing DFT [34,35], with norm-conserving pseudopotentials and a plane-wave basis set. The ionic potential was modeled using Optimized Norm-Conserving Vanderbilt (ONCV) pseudopotentials [45]. The exchange-correlation effects were treated within the generalized gradient approximation (GGA) using the Perdew-Burke-Ernzerhof (PBE) functional [46], supplemented by the vdW-D3 correction [47] to account for long-range van der Waals interactions between monolayers. Spin-orbit coupling (SOC) was included in all calculations, and the *sp* semicore states of the transition metal atoms were explicitly treated as valence electrons [13,26,48]. This approach is essential for accurately capturing the exchange contribution to the self-energy term in *GW* calculations.

For all systems, we adopted a plane-wave energy cutoff of 70 Rydberg (Ry) for the electronic wave function expansion and employed a $12 \times 12 \times 1$ Monkhorst-Pack [49] k-point mesh for BZ sampling. A vacuum layer of 27 Åwas introduced along the out-of-plane direction to prevent spurious interactions between periodic images.

Structural relaxations were performed until the atomic forces were reduced below 0.01 eV/Å, and the energy convergence threshold was set to 10^{-5} eV. These criteria ensured that the residual stress remained below 0.01 kbar.

Since DFT, in its local and semi-local approximations, often underestimates band gaps due to its limited treatment of electron-electron interactions, we employed the more accurate *GW* approximation to obtain reliable quasiparticle energies. Specifically, the G_0W_0 approach was used to correct the Kohn-Sham eigenvalues by solving the Dyson equation [36–39], thereby renormalizing the band gaps to values in better agreement with experimental measurements. The quasiparticle (QP) energies (single-particle excitation energies) were computed within the G_0W_0 by using the linearized quasiparticle equation [50]:

$$\varepsilon^{n\mathbf{k}}_{\mathbf{QP}} = \varepsilon_{n\mathbf{k}} + Z_{n\mathbf{k}}\langle n\mathbf{k}|\Sigma(\varepsilon_{n\mathbf{k}}) - v_{xc}|n\mathbf{k}\rangle \,, \tag{1}$$

where $\epsilon_{n\mathbf{k}}$ and v_{xc} describe the Kohn-Sham eigenvalues and exchange-correlation potential, respectively, evaluated over $|n\mathbf{k}\rangle$ Kohn–Sham eigenstates. The normalization factor $Z_{n\mathbf{k}}$ is defined as

$$Z_{n\mathbf{k}} = \left[1 - \langle n\mathbf{k}|\frac{\partial\Sigma(\omega)}{\partial\omega}|n\mathbf{k}\rangle|_{\,\omega=\epsilon_{n\mathbf{k}}}\right]^{-1}. \tag{2}$$

This linearized form of the quasiparticle equation is routinely used in GW calculations and is valid for materials that do not exhibit very small band gaps, such as the systems considered in this work.

The expectation values of the self-energy are written as

$$\Sigma_{nk} = -\int \frac{d\omega'}{2\pi i} e^{i\omega' 0^+} \left\langle \phi^{KS}_{n\mathbf{k}} \middle| G(\omega+\omega')W(\omega') \middle| \phi^{KS}_{n\mathbf{k}} \right\rangle . \tag{3}$$

The Green functions, G, are constructed using the DFT eigenfunctions, $\phi^{KS}_{n\mathbf{k}}$, and their corresponding eigenvalues, $\epsilon_{n\mathbf{k}}$. The dynamical screening effects in the self-energy, W, are treated within the generalized plasmon-pole model [51]. In the *GW* self-energy calculations, cutoff energies of 70 and 12 Ry are applied for the exchange and correlation components, respectively, and up to 350 empty states are included in the summation over unoccupied states. A uniform k-point grid of $27 \times 27 \times 1$ is utilized for both monolayers and bilayer heterostructures to ensure accurate BZ sampling [see Supplemental Material [52] for details]. To avoid numerical divergence of the Coulomb potential at small $\mathbf{q}$ which creates convergence problems in the QP corrections of 2D

semiconductors, we used the so-called random integration method [50].

Starting from the Kohn-Sham wave functions and the quasiparticle energies, the absorption spectra are calculated on the level of BSE formalism [38–41]:

$$(E_{c\mathbf{k}} - E_{v\mathbf{k}})A^{\lambda}_{vc\mathbf{k}} + \sum_{\mathbf{k}'v'c'} \langle vc\mathbf{k}|K_{eh}|v'c'\mathbf{k}'\rangle A^{\lambda}_{v'c'\mathbf{k}'} = E_{\lambda}A^{\lambda}_{vc\mathbf{k}}, \tag{4}$$

where $A^{\lambda}_{vc\mathbf{k}}$, E_{λ}, and K_{eh} are the expansion coefficients of the excitons in electron-hole basis, the eigenenergies, and the kernel of the BSE, respectively.

Here, the excitonic Hamiltonian is constructed in the basis of electron-hole pairs, accounting for direct excitations at a given momentum $\mathbf{k}$ from a valence band state with quasiparticle energy $E_v(\mathbf{k})$ to a conduction band state with quasiparticle energy $E_c(\mathbf{k})$. The interaction kernel, K_{eh}, incorporates both the repulsive unscreened exchange interaction (V) and the attractive screened Coulomb interaction (W) between electron-hole states. These interactions can give rise to discrete excitonic states below the onset of the quasiparticle continuum. In the absence of electron-hole interactions i.e., when the interaction kernel K_{eh} is neglected, the optical excitations reduce to independent electron-hole pair transitions. In this case, the optical response of the system is governed by single-particle interband transitions without excitonic effects.

The optical absorption spectrum is given by the imaginary part of the dielectric function, $\epsilon(\omega)$, and can be calculated as

$$\epsilon(\omega) = 1 - \sum_{\mathbf{k}vc}\sum_{\mathbf{k}'v'c'} \lim_{\mathbf{q}\to 0} \frac{8\pi}{|\mathbf{q}|^2 \Omega N_q} \rho^{*}_{vc\mathbf{k}}(\mathbf{q}, \mathbf{G}) \times \rho_{v'c'\mathbf{k}'}(\mathbf{q}', \mathbf{G}') \sum_{\lambda} \frac{A^{\lambda}_{vc\mathbf{k}}(A^{\lambda}_{v'c'\mathbf{k}'})^{*}}{\omega - E_{\lambda}}, \tag{5}$$

where ρ_{nm} are defined as [50]

$$\rho_{nm}(\mathbf{k}, \mathbf{q}, \mathbf{G}) = \langle n\mathbf{k}|e^{i(\mathbf{q}+\mathbf{G})\cdot\mathbf{r}}|m\mathbf{k}+\mathbf{q}\rangle \ . \tag{6}$$

The optical transitions are characterized by the dipole matrix elements, $\langle c\mathbf{k}|p_i|v\mathbf{k}\rangle$, which describe the coupling between valence and conduction states. Here, p_i denotes the i-th component of the momentum operator. The excitonic states are defined by their excitation energies, E_{λ}, and corresponding amplitudes, A^{λ}_{vck}. To achieve convergence in the solution of the BSE, calculations were performed on the same k-point grid used in the *GW* calculations. The interaction kernel in the BSE was constructed using six conduction bands and six valence bands. Further details on the convergence of BSE calculations are provided in the Supplemental Material [52]. A Lorentzian broadening of 0.15 eV was applied to simulate the absorption spectra. In both *GW* and BSE calculations, the Coulomb interaction was truncated to eliminate spurious interactions between periodic images of the layers [53].

III. RESULTS AND DISCUSSION

A. Structural properties

WSe_2 and MoS_2 monolayers are transition-metal dichalcogenides (TMDs) made up of two Se (S) layers and hexagonal planes of W (Mo) atoms covalently bound to them in a trigonal prismatic coordination. Through vertical stacking of these two-dimensional crystals, a vdW structure is created, forming the heterobilayer WSe_2/MoS_2. Despite rotational alignment during fabrication, the small in-plane lattice mismatch (3-4%) between WSe_2 and MoS_2, generates Moiré patterns [22,54,55].

An atomic model of the R-type Moiré supercell is depicted in Fig. 1(a), which follows the nomenclature of Ref. [22] (itself adapted from conventional stacking terminology [54,55]) and highlights three local energy-minimum configurations labeled AA, AB_W, and AB_{Se}. In Fig. 1(b), we show the atomic arrangements for these three local alignments. These arrangements correspond to the three stable energy-minimized states found in the heterobilayer, and the interaction between lattice mismatch and interlayer registry is reflected in the Moiré supercell geometry. Two local energy-maximum bridge configurations (Br and Br_2) are also accessible. These intermediate structures are produced through translation of the MoS_2 lattice with respect to WSe_2 between neighboring AB_{Se} sites. These metastable structures spontaneously transformed into one of these three stable phases upon relaxation. Therefore the present study focuses only on the most stable configurations, ensuring that our analysis is representative of physically realizable structures and relevant to experimental conditions. The arrangement of local atomic structures within these stacking configurations leads to a modification of interlayer forces, resulting in out-of-plane corrugations and spatially dependent distances between layers within the heterostructure [22,54,55].

To model each labeled site in Fig. 1, a 1×1 WSe_2/MoS_2 heterobilayer unit cell was constructed, containing six atoms. The lattice constant was set to the average of the monolayer WSe_2 and MoS_2 lattice parameters, preserving the hexagonal symmetry inherent to the parent monolayers. The three stable stacking configurations examined here (AA, AB_W, and AB_{Se}) were predicted theoretically [22], and observed experimentally in samples grown by chemical vapor deposition (CVD) [22,56]. The AA stacking is constructed by positioning Mo atoms over W atoms and S atoms in one layer over Se atoms in the layer beneath with zero degree rotation of WSe_2 with respect to the MoS_2 layer. The difference in the local atomic registry between AA and AB stackings resides in the lateral alignment of the chalcogen atoms. AB_{Se} (AB_W) means that the hexagonal lattices of the metal atoms in the two monolayers are stacked in an AB manner with the Mo (W) atoms in one layer are covered by chalcogen atoms in the other layer. In other words, W atoms is covered by S atoms in AB_{Se} and Mo atom is covered by Se atoms in AB_W. Consequently, interlayer coupling would be significantly influenced as we will see later in the paper.

According to the nomenclature of the previous study [55], AA is an eclipsed stacking. The AB bernal stacking can be obtained by simple transformations from AA configuration by horizontal layer sliding. AB is staggered with metal atoms of one layer aligned with chalcogen atoms of the other layer and can be obtained by shifting the WSe_2 layer with respect to MoS_2 layers by $a/\sqrt{3}$, where a is the lattice parameter. Both AA and AB stacking orders are of R-type.

We computed the lattice constants, interlayer distances, and bond lengths for monolayers and bilayers. The lattice constant of the heterobilayer is approximately 3.23 Å,

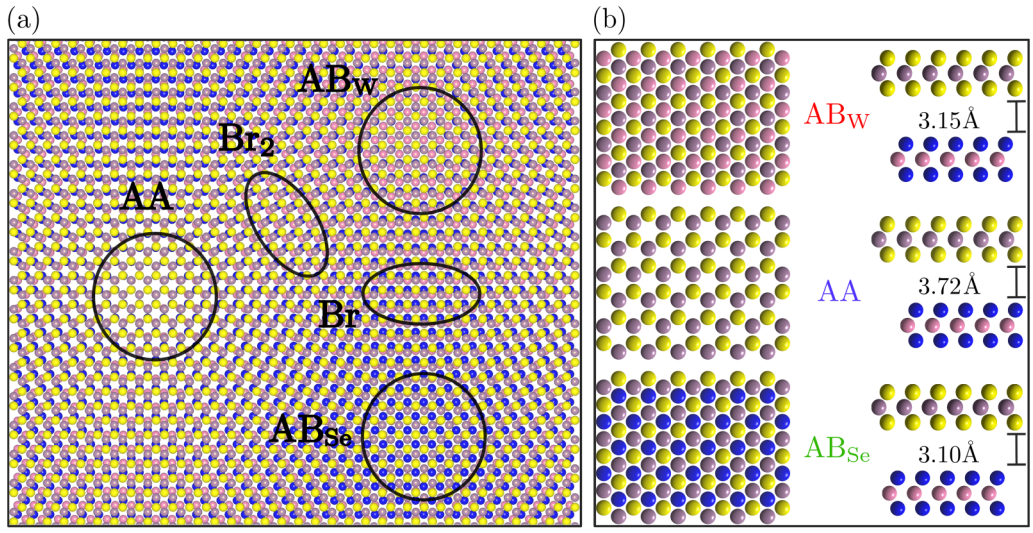

FIG. 1. (a) Schematic model of the Moiré pattern on an R-stacked WSe_2/MoS_2 heterobilayer. (b) Top and side views of the atomic models for AA, AB_W, and AB_{Se} registries zoomed in on a unit cell of the moiré pattern.

achieved through a 2.7% in-plane compression of the monolayer WSe_2 and a 1.5% expansion of the monolayer MoS_2 to enforce commensurability. This approach, often used to model vdW heterostructures with small unit cells, minimizes artificial strain while preserving a commensurate supercell for periodic boundary conditions. Relaxation of the internal coordinates and interlayer spacing yields equilibrium bond lengths, bond angles, and interlayer distances, with negligible residual forces and stresses. In the three stacking configurations, the average Mo-S and W-Se bond lengths are 2.425 and 2.528 Å, respectively. These correspond to compressions of about 0.3% (Mo-S) and 0.8% (W-Se) relative to their isolated monolayer values. The minor deviations in lattice parameters and bond lengths from those of the parent monolayers are consistent with weak interlayer interactions. Our results align closely with prior theoretical and experimental studies [22,57–60].

To evaluate the relative stability of the three configurations, we calculated their formation energies. Contributions from phonons were omitted due to the dominance of weak vdW interactions [61], and zero-point vibrational effects were assumed to be negligible [62]. The AA stacking configuration exhibits a formation energy of −223 meV/cell, which is only 0.06 and 0.07 meV lower than those of AB_W and AB_{Se}, respectively. Although AA stacking is the most stable configuration, the very small energy differences between the three configurations indicate that they have comparable thermodynamic stability.

The interlayer distance d, which is the distance between the constituent layers [see Fig. 1(b)], is calculated to be approximately 3.72, 3.15, and 3.10 Å for AA, AB_W, and AB_{Se}, respectively. This distance is largest when the S atoms are directly aligned above the Se atoms, as this is the case in the AA registry. This occurs due to increased Pauli repulsion between the overlapping electron clouds localized around these atoms. On the contrary, in AB stacking configurations, the interlayer distance d is reduced due to the alignment of the metal atoms in one layer with the chalcogen atoms in the adjacent layer. This alignment strengthens the electrostatic attraction, resulting in a reduced separation between the Se and S atomic layers.

B. Electronic properties

Figure 2 shows the DFT and G_0W_0 band structures for monolayer WSe_2 and MoS_2 and their corresponding heterostructures. Consistent with prior studies [26,48,59,63,64], both WSe_2 and MoS_2 monolayers exhibit direct band gap semiconducting behavior at their equilibrium geometries under DFT and G_0W_0 treatment [see Fig. 2(a)], a direct consequence of inversion symmetry breaking (group of symmetry D_{3h}) inherent to their honeycomb lattice structures [4,7]. Our mean field theory calculations reveal fundamental gaps of 1.62 eV (MoS_2) and 1.27 eV (WSe_2) at the K point, with doubly degenerated valence bands predominantly of localized $d_{x^2-y^2}$ character. Spin-orbit coupling induces a splitting of the valence band into two uppermost valence bands (VB and VB-1), with energy separations of 457 meV in WSe_2 and 147 meV in MoS_2, consistent with prior theoretical and experimental reports [48,59,60,64–67]. Many-body G_0W_0 corrections substantially increase these fundamental gaps to 2.72 and 2.17 eV, respectively, showing excellent consistency with established theoretical references [26,48,64,65,67,68]. Discrepancies with values available in the literature likely originate from variations in computational parameters, particularly exchange-correlation functional implementations and unit cell optimizations. In this work, the energy zero for each computational method (DFT and GW) was set consistently to its own internal reference, avoiding any artificial alignment that could mask the fundamental many-body corrections. This approach is crucial as GW theory typically shifts conduction bands upward and valence bands downward, increasing the band gap relative to DFT; a visual similarity in absolute band positions often arises only from a specific alignment choice (vacuum level, Fermi energy, or a band edge). To ensure the reliability of the quasiparticle results, we tested convergence with respect to all critical parameters, including the number of unoccupied bands, dielectric cutoff, and k-point sampling,

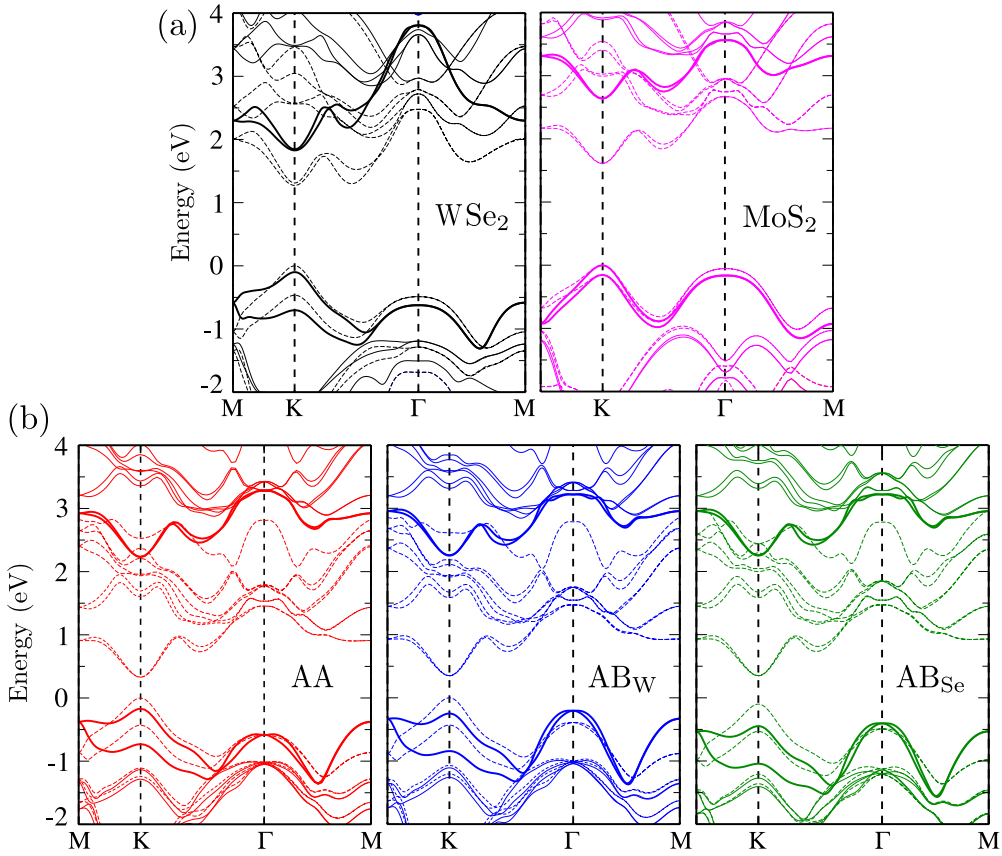

FIG. 2. Band structures calculated DFT (GGA, thin dashed lines) and the G_0W_0 approximation (thick solid lines). (Top) Monolayer MoS_2 (left) and monolayer WSe_2 (right). (From left to right in the bottom panel) AA, AB_W, and AB_{Se} stacked WSe_2/MoS_2 heterobilayers.

and obtained an accuracy better than 0.05 eV (see Figs. S1–S3 and Table 1 in Ref. [52]).

For heterobilayers [Fig. 2(b)], DFT calculations reveal direct band gaps at the K point, with a twofold degenerate valence band. The computed band gaps are 0.33 eV (AA), 0.35 eV (AB_W), and 0.45 eV (AB_{Se}), in agreement with existing literature [65,66]. Crucially, the band-gap tunability with stacking order suggests a pathway to tailor electronic properties via layer arrangement. Near the K point, hybridization effects dominate the band edges, driven by the d orbital contributions of the metal atoms: the valence band arises from hybridization of W $5d_{x^2-y^2}$ and $5d_{3z^2-r^2}$ orbitals, while the conduction band is predominantly derived from Mo $4d_{3z^2-r^2}$ orbitals. To model the local configurations, we employed 1×1 WSe_2/MoS_2 unit cells with a fixed in-plane lattice constant of 3.23 Å, corresponding to the average of the unstrained monolayer lattice parameters. In this configuration, the MoS_2 layer experiences tensile strain, while the WSe_2 layer is under compressive strain. Although the influence of this strain on the interlayer interactions is expected to be minor, we assessed its effect by comparing the electronic band structures of unstrained and strained monolayers. Our calculations indicate that the band gap of monolayer WSe_2 increases by approximately 3%, while the band gap of monolayer MoS_2 decreases by about 7%. These variations, while non-negligible, do not alter the optical response of the heterostructure. Indeed, since excitonic properties in TMDs are primarily governed by the relative band-edge alignment and exciton binding energies, their behavior is expected to be robust against the modest strains introduced by lattice-constant averaging. Theoretical studies have shown that small biaxial strain leaves effective masses and binding energies nearly unchanged, so that excitonic transition energies closely follow the strain-induced shifts of the underlying electronic band edges [69,70]. Consequently, the essential nature of excitons in the WSe_2/MoS_2 heterobilayer is preserved. This conclusion is consistent with experimental observations on strained monolayers and bilayers, where moderate biaxial strain produces only modest shifts (tens of meV per percent strain) in excitonic resonances without altering their qualitative character [71–73].

Interlayer vdW interactions in WSe_2/MoS_2 heterobilayers yield a type-II band alignment, wherein the valence band and the conduction band are localized on distinct monolayers. This spatial separation of charge carriers generates momentum-direct charge-transfer excitons, with holes confined to WSe_2 and electrons to MoS_2. Such a mechanism profoundly influences optical properties and presents compelling opportunities for optoelectronic applications, including excitonic devices and light-harvesting systems. At the DFT level, heterobilayer band gaps are typically smaller than those of the individual monolayers due to interlayer interactions and orbital hybridization between the two layers. Specifically, the $d_{3z^2-r^2}$ orbitals of W and Mo atoms overlap across the layers, modifying the band structure through interlayer coupling. These d orbitals are more localized than s and p orbitals and often exhibit strong electron-electron repulsion,

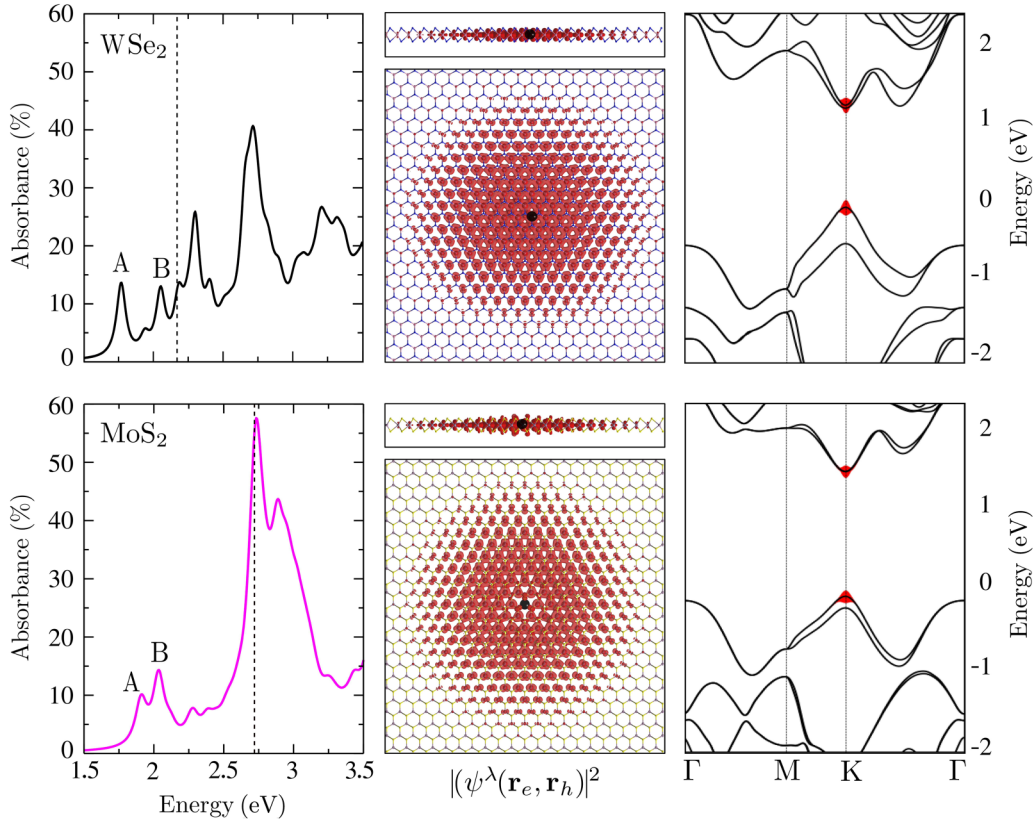

FIG. 3. (Left) Optical absorption spectra of WSe_2 and MoS_2 single layers, given by the absorbance. QP band gaps are marked with vertical dashed lines, and the labels indicate the peaks associated with the A and B excitons. (Middle) Side view and top view of exciton A charge density. (Right) Reciprocal-space distribution of exciton A. The sizes of the red patches are indicative of the weights of the involved QP states.

leading to huge electronic correlation effects. Standard DFT, especially with local or semilocal functionals such as GGA, often struggles to capture these correlation effects accurately, particularly for the localized *d* electrons. Consequently, DFT may not account for the strong Coulomb interactions within the *d* orbitals, which reduces the energy difference between the valence 5*d* bands and the conduction 4*d* bands, thereby leading to a smaller fundamental band gap in the bilayer system compared to the parent monolayers.

Moreover, accounting for electron-electron interactions through a G_0W_0 calculation significantly enhances the band gap by over 80%. This result aligns closely with prior theoretical studies [65]. Interestingly, the AA stacking configuration retains its direct band gap character at *K*, while AB stackings transition to indirect band gap materials upon the inclusion of electron-electron self-energy. The origin of this difference is the interlayer interaction. While the CB remains at the *K* point, the VB shifts from *K* to Γ. This shift can be explained by the differences in the effective mass of the charge carriers at these high-symmetry points. The electron-electron interactions modify the effective mass, which affects the energy dispersion near the band edges. In AB stacking configurations, the effective mass at the Γ point would be lighter compared to the *K* point making it energetically favorable for the VB to relocate, resulting in an indirect band gap. The AA registry is predicted to exhibit a direct band gap of 2.40 eV, highlighting its potential for optoelectronic applications due to its suitability as an efficient light emitter. For AB_W and AB_{Se} registries, direct band gaps of 2.50 and 2.70 eV are observed at the *K*-point, while indirect gaps of 2.44 eand 2.65 eV are found between the Γ and K points. The small difference between the direct and indirect band gaps suggests that these materials may also be promising for optoelectronic applications, as they remain effective light emitters. The large quasiparticle corrections to the PBE band gap originates from the enhancement of the electron-electron interaction and the weakening of the screening response in two-dimensional materials. Such a low screening gives rise to bound excitons with large binding energies. The bilayers possess the factor group C_{3v}, which also lacks inversion symmetry. This absence of inversion symmetry, combined with SOC, results in valence band splitting. The values are 562, 594, and 600 meV for AA, AB_W, and AB_{Se}, respectively, demonstrating a marked enhancement compared to monolayer counterparts. This increased splitting may arise from interlayer coupling, which introduces an additional contribution to the spin-orbit interaction beyond monolayer effects.

C. Optical absorption spectra

In Fig. 3, there the optical absorption spectra of monolayer WSe_2 (top left panel) and MoS_2 (bottom left panel) are shown, revealing striking similarities in their low-energy excitonic features. All systems exhibit a characteristic double-peak structure at the absorption onset (denoted as A and B excitons). These spectral features come from strong interac-

tions between electrons that create tightly bound excitons, which mainly influence how the material responds to light. The energy splitting between A and B excitons reflects the SOC effects in the valence band. Monolayer MoS_2 exhibits a splitting of 114 meV, while WSe_2 shows a larger splitting of 183 meV, attributed to the heavier tungsten atom enhancing SOC. The A (B) exciton is found at 1.76 eV (1.93 eV) and 1.91 eV (2.03 eV) in MoS_2 and WSe_2 monolayers, respectively, with binding energies of 0.81 eV (A) and 0.61 eV (B) for MoS_2, and 0.40 eV (A) and 0.23 eV (B) for WSe_2, which values significantly exceed those in bulk semiconductors. Our results are in good agreement with previous calculations [63,74] and experiments [75]. This enhancement stems from reduced dielectric screening in atomically thin layers, which amplifies Coulomb interactions.

The lowest-energy exciton is optically forbidden in these structures, despite broken inversion symmetry. While the presence or absence of inversion symmetry in a crystal fundamentally dictates the optical activity of excitonic states, additional factors such as SOC and band-edge orbital symmetries determine whether the lowest-energy exciton is optically active (bright) or optically inactive (dark). This distinction becomes apparent when comparing the excitonic behavior of these monolayers with that of hBN [76], despite both of which crystallize in the non-centrosymmetric D_{3h} point group. In hBN, the weak SOC and $\pi \rightarrow \pi^*$ character of the band edges ensure that the lowest exciton remains bright, as the dipole-allowed transition is symmetry-permitted. In contrast, monolayer WSe_2 and MoS_2 exhibit strong SOC, which lifts the spin degeneracy of both valence and conduction bands, giving rise to a spin-forbidden exciton that can lie below the bright A exciton in energy. Despite the lack of inversion symmetry, which typically permits dipole transitions, the excitonic ground state in monolayer WSe_2 and MoS_2 can therefore be dark. These observations drive home that, while inversion symmetry sets the general optical selection rules, the fine structure of excitonic states and the relative ordering of bright and dark excitons depend sensitively on SOC strength, orbital hybridization, and symmetry of the band edges.

In the middle panel of Fig. 3, we plot the squared magnitude of the real-space wave function for the exciton corresponding to peak A in monolayer WSe_2 and MoS_2, with the hole localized near a W atom in WSe_2 and a Mo atom in MoS_2. The spatial profile of this exciton exhibits a nearly circular symmetry, closely resembling the 1*s* orbital of a 2D hydrogenic system. In both monolayers, the electron density for the exciton in both materials predominantly localizes on nearest-neighbor metallic atoms adjacent to the hole, reflecting restricted spatial charge separation. This pronounced overlap between electron and hole wave functions indicates shorter excitonic radiative lifetimes. The electron density profiles exhibit rapid spatial decay, characteristic of tightly bound electron-hole (*e*-*h*) pairs. Notably, the exciton MoS_2 displays a more localized charge distribution compared to its counterpart in WSe_2, consistent with its highest binding energy. This trend indicates a direct correlation between binding energy and spatial delocalization: reduced binding energy corresponds to progressively extended excitonic wave functions.

As illustrated in the right panel of Fig. 3, this exciton originates from electronic transitions involving the in-plane $d_{z^2-r^2}$ orbital in the VB band and the out-of-plane d_{z^2} orbital in the CB of the metal atoms. It is important to note that the real-space wave function of exciton B is spatially indistinguishable from that of exciton A. This equivalence arises from the conservation of spin as a good quantum number at the K and K' valleys [18]. Despite spin-orbit-induced splitting in the valence bands, the spatial components of the valence band wave functions remain identical across both valleys. Consequently, peaks A and B, which stem from transitions between the spin-orbit-split valence bands (VB, VB-1) and the lowest conduction band (CB) at the K and K' valleys, respectively, share identical spatial wave functions. Although these excitons originate from distinct valleys and exhibit different spin configurations, their spatial structures are invariant under spin conservation, reflecting the symmetry imposed by valley-dependent spin selection rules.

Beyond the A and B peaks, the absorption spectrum contains contributions from weakly bound electron-hole pairs. At higher energies, the absorption increases abruptly, being in accordance with direct band-to-band transitions, where excitonic effects become negligible. Subtle variations in peak shapes and spectrum breadth across materials arise from differences in carrier effective masses, SOC strength, and dielectric screening mechanisms. Our findings exhibit excellent agreement with prior experimental and theoretical studies [25,26,64,67], validating the robustness of the observed trends.

We now turn to the excitonic properties of heterobilayers. In Fig. 4, we display the real-space distributions of three exciton types found in different stacking configurations. The first type is a 2D exciton, with the electron and the hole settling in the same layer. These excitons can be further classified into MoS_2-like exciton (2D-MoS_2) and WSe_2-like exciton (2D-WSe_2) states in the in-plane direction. The second type is the charge transfer (CT) excitons, where the electron and the hole sit on different layers. The third category is the three-dimensional (3D) exciton, where the hole is confined to one layer while the electron is distributed across both layers.

In all cases, the excitonic wave functions exhibit trigonal symmetry, which mirrors the hexagonal lattice symmetry of the monolayer. Moreover, their charge distributions display extended features, indicative of localization in reciprocal space (see Fig. 5). The stacking-dependent structural and electronic properties are reflected in different optical responses. Specifically, the AA and AB_{Se} stacking arrangements accommodate the three exciton types, whereas the AB_W configuration supports only 2D and CT excitons. These excitonic characteristics are intimately linked to the symmetry and atomic registry of each stacking arrangement. To explain these features, we analyze the electronic band structures and optical spectra, emphasizing their interplay with the underlying atomic geometry.

In the eclipsed AA stacking, all atoms in the two nonequivalent layers align perfectly, with Mo atoms positioned directly above W atoms and S atoms directly above Se atoms. In contrast, the AB staggered stacking adopts a hollow-site registry, wherein alternating atoms occupy hollow sites. Specifically, in the AB_{Se} stacking, Mo and Se atoms are located at hollow positions, whereas in AB_W, W, and S atoms occupy these sites [see Fig. 1(b)]. These different lateral registries result

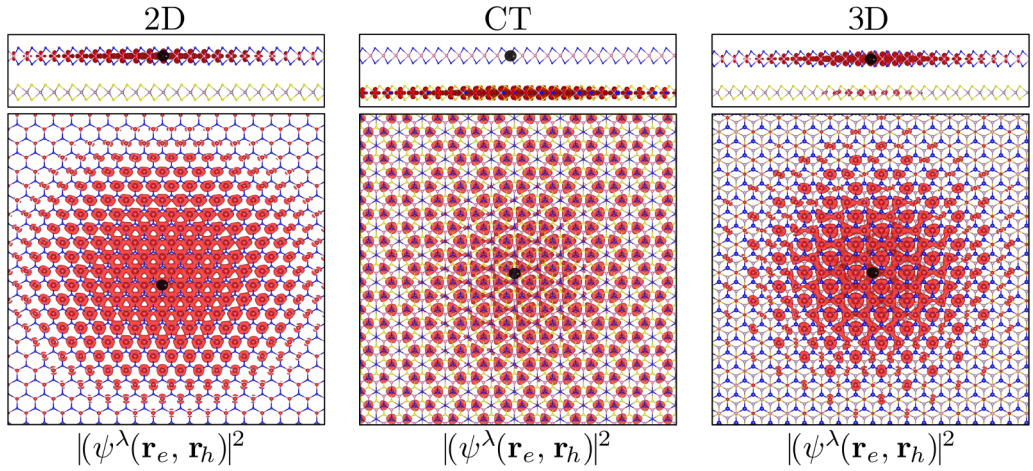

FIG. 4. Side view and top view of exciton of charge densities (side and top view) of the three types of excitons that can emerge in WSe_2/MoS_2 heterobilayer upon different stacking configurations. From left to right: a 2D exciton (AA), where the electron and hole reside within the same layer; a charge-transfer (CT) exciton (AB_W), with the electron and hole pinned in different layers, and 3D exciton (AB_{Se}) where the hole is located in one layer while the electron is distributed across both layers. The hole is indicated by a black dot, while the electron distribution is depicted by the red isosurface.

in varying electronic structures [see Fig. 2(b)], which in turn influence the optical spectra (see Fig. 5). In the following discussion, we examine how these structural properties govern the formation of various $e - h$ pairs.

In Fig. 5, we display the optical spectra (left panel) together with the band structures (right panel) (see also Fig. S5 in Ref. [52]). Our calculations reveal a significant redistribution of oscillator strength accompanied by a pronounced redshift of the absorption spectrum. Notably, we observe the emergence of strong excitonic resonances below the single-particle continuum onset, along with a large manifold of optically forbidden excitonic states below the onset of single-particle transition continuum

First, we begin by examining the 2D exciton depicted in Fig. 4 (see also Fig. S6 left panel in Ref. [52]). This bound electron-hole (e-h) pair is observed across all three stacking arrangements, manifesting as the first bright excitons in each registry. In the AA configuration, this exciton is intralayer in nature and resides exclusively in the WSe_2 monolayer. No corresponding 2D exciton localized in MoS_2 monolayer is found within the energy window of the band gap. It is non-degenerate and emerges at an energy of 2.17 eV, with a binding energy of 0.23 meV. Similar to the A exciton in monolayers, its wave function envelope is nearly azimuthally symmetric. This exciton marked in the spectrum of Fig. 5 arises from transitions between the VB and the CB + 3 states near the band extrema at the high-symmetry K point, as shown in Fig. 5 (right panel). Since both the VB and the CB + 3 originate from orbitals localized in the W-based monolayer, hole localization within this layer confines the electronic charge density to the same layer, confirming its 2D character. In the AB stacking configuration, this behavior is reversed: the lowest-energy 2D exciton is localized in the MoS_2 monolayer, while no 2D exciton residing in WSe_2 monolayer is found. We emphasize that, although this type of exciton appears in both AB_{Se} and AB_W registries, it is different in each case due to its stacking-dependent character. Due to the symmetry of the lattice, it exhibits a twofold degeneracy. In the AB_W configuration, it appears at 2.16 eV with a binding energy of 0.27 eV, while in the AB_{Se} configuration, it emerges at 2.07 eV with a notably high binding energy of 0.58 eV. In both cases, these excitons arise from transitions between the VB-2/VB-3 and CB/CB + 1 states at the K point. The second 2D exciton in AB_W is located at 2.29 eV with a binding energy of 0.15 eV, originating from transitions between VB-3 and CB/CB + 1. In AB_{Se}, two further 2D excitons are found at higher energies: the first at 2.18 eV with a binding energy of 0.47 eV, arising from transitions between VB-3 and CB + 1; and the second at 2.20 eV with a binding energy of 0.45 eV, arising from transitions between VB–2 and CB. The electron density associated with the 2D exciton is primarily localized on the nearest-neighbor metal atoms adjacent to the hole, resulting in restricted spatial charge separation and, consequently, reduced excitonic radiative lifetimes.

Next, we examine the CT excitons, also depicted in Fig. 4. These doubly degenerate optically forbidden excitons are also found in all stacking configurations, appearing as the first exciton in all registries. In AA, the CT exciton marked in the spectrum of Fig. 4 emerges at about 2.28 eV. It is twofold degenerate, with a binding energy of 0.12 eV, and originates from interband transitions between the VB and the CB at the high-symmetry K point. In the spectrum of AB_W configuration, the CT exciton observed at 2.16 eV, has a binding energy of 0.28 eV, and arises from transitions between the VB and CB near K point. In the AB_{Se} arrangement, the CT exciton located at 2.27 eV has a binding energy of 0.38 eV. It originates from transitions between the VB and the CB/CB + 1 at the K point. Here, the hole is localized on the W $d_{z^2-y^2}$ orbitals and the corresponding electronic wave functions are spread over metallic atoms belonging to MoS_2 layer. Further details are provided in Ref. [52].

The final exciton type, 3D, is found exclusively in AA and AB_{Se} stacking configurations, appearing as the second bright exciton in AA. It is a doubly degenerate exciton and appears at 2.32 eV with a binding energy of 0.08 eV, stemming from transitions between the VB and CB + 3 states at the

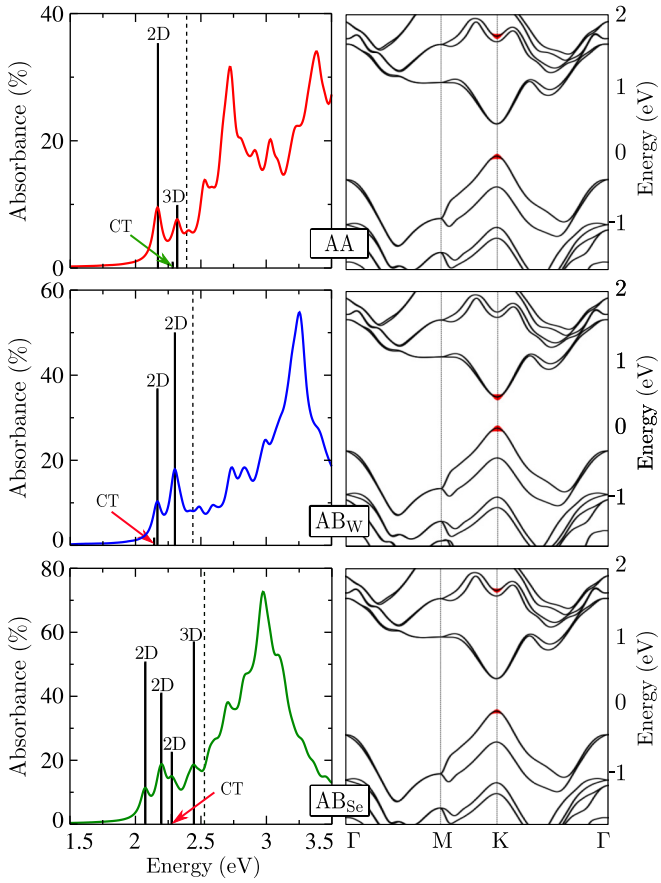

FIG. 5. (Left) Optical absorption spectra, given by the absorbance in AA, AB_W, and AB_{Se} registries. The dashed line indicates the direct QP gap. (Right) Band (DFT) contributions to the excitations marked in the spectra. The labeling follows the nomenclature of Fig. 4: the 2D exciton (AA stacking), the charge-transfer (CT) exciton (AB_W), and the 3D exciton (AB_{Se}). The sizes of the red patches are indicative of the weights of the involved states. The 2D exciton of AA stacking exhibits WSe_2-like character, whereas those of the AB stacking are of MoS_2-like.

high-symmetry K point. The wave function of this exciton is delocalized over the whole space and displays extended features. In AB_{Se}, the equivalent exciton appears at 2.44 eV with a binding energy of 0.21 eV. It is also degenerate and originates from transitions between the VB and CB + 3 states in the vicinity of the K point. Interestingly, we observe a characteristic dumbbell-like distribution of electron density around each W atom in all exciton types. This feature arises from the d orbitals of individual metallic atoms and persists across all stacking configurations (see Fig. 5 and Fig. S6 in Ref. [52]).

The variation in exciton binding energies among the three configurations (AA, AB_{Se}, and AB_W) stems from the interplay between interlayer orbital hybridization and interlayer distance. AA stacking exhibits the strongest orbital hybridization due to direct metal (Mo/W) and chalcogen (S/Se) alignment, which enhances dielectric screening and reduces binding energy. Although this configuration exhibits a slightly larger interlayer separation, which would reduce screening and increase binding energy, the dominant effect of the pronounced hybridization-induced screening yields the lowest binding energy among the three stackings.

In AB stackings (AB_{Se} and AB_W), the metal atoms are eclipsed by chalcogen atoms (W by S in AB_{Se}, Mo by Se in AB_W), which reduces direct interlayer orbital hybridization, and thereby diminishes dielectric screening. At the same time, the shorter interlayer distance enhances the bare Coulomb interaction between the electron and hole. The combined effect of reduced screening and increased Coulomb attraction leads to larger exciton binding energies compared to the AA configuration.

The difference between AB_{Se} and AB_W originates from the chemical asymmetry of the interface. In AB_{Se}, the presence of the more electronegative sulfur atom at the W-S interface creates a stronger interfacial dipole and less effective local screening, whereas in AB_W, the larger and more polarizable selenium atom at the Mo-Se interface provides somewhat greater screening. As a result, the exciton binding energy is slightly higher in AB_{Se} than in AB_W, reflecting the modulation of the dielectric response by the interfacial chemistry.

The absence of 3D excitons in the AB_W stacking configuration is due to a complex interplay of symmetry constraints, interlayer hybridization effects, and orbital-specific interactions. In the AB_W registry, where W and S atoms occupy hollow sites, the resulting potential landscape and orbital overlap differ fundamentally from the AB_{Se} case. The 3D excitons observed in AA and AB_{Se} stackings originate from transitions to highly delocalized CB + 3 states that require strong interlayer hybridization of Mo-d and W-d orbitals, a condition that is apparently not satisfied in AB_W due to the more localized nature of W-derived states near the Fermi level. This localization originates from both the stronger d-orbital confinement of W atoms and the particular nodal structure of the electronic wavefunctions in AB_W, which restricts charge delocalization across the heterobilayer. Furthermore, the AB_W band structure exhibits significant renormalization of higher conduction bands, with CB + 3 states either shifting outside the relevant energy window or becoming optically forbidden due to registry-dependent selection rules. This difference with the AB_{Se} stacking configuration highlights how variations in the atomic registry can dramatically modify the dimensionality of excitonic states. The absence of 3D excitons in AB_W clearly shows how stacking symmetry can be an effective way to control excitons in van der Waals heterostructures.

The categorization of excitons into distinct dimensional classes (2D, CT, 3D) provides a critical framework for understanding their fundamental physics and tailoring material properties for specific optoelectronic applications, as seen in related material systems [15,77,78]. Dimensionality plays the biggest role in shaping exciton properties, including binding energy, diffusion length, and dissociation efficiency. Consequently, strongly bound 2D excitons are ideal for light-emitting devices requiring high radiative recombination rates [4,7], while the more delocalized nature of CT and 3D excitons makes them better suited for charge separation in photovoltaics [79,80]. The validation of these theoretical predictions and the experimental distinction between these species are therefore crucial. A powerful approach involves a combination of advanced spectroscopies. Temperature-dependent photoluminescence (PL) can directly probe binding

energies, where 2D excitons were found to resist quenching, unlike 3D excitons, which dissociate easily [81–84]. Transient absorption spectroscopy (TAS) will be essential to resolve their distinct dynamical fingerprints: fast, localized decay for 2D excitons [77,83], longer lifetimes sensitive to the dielectric environment for CT states [85,86], and rapid dissociation into free carriers for 3D excitons [87]. Stark spectroscopy (electroabsorption) can distinguish excitons through their polarizability: CT and 3D excitons show strong Stark shifts and line broadening, while 2D excitons respond much more weakly [88,89]. These measurements provide a direct way to test the predicted coexistence of excitonic states in heterobilayers, offering clear support for our theoretical framework.

It is noteworthy that the close energetic alignment between 2D and CT excitons provides an efficient non-radiative relaxation pathway: photoexcited 2D excitons undergo ultrafast charge transfer to form lower-energy CT states [90]. This process rapidly reduces the 2D exciton population available for direct radiative recombination, thereby quenching its emission. However, because CT excitons exhibit strong spatial electron-hole separation, their radiative recombination rate is drastically reduced, making them inherently long-lived [77,86]. As a result, while the radiative channel is quenched, the overall exciton population acquires an extended lifetime as excitons accumulate in this long-lived dark state reservoir. Such a mechanism, where efficient charge transfer simultaneously suppresses intralayer luminescence and generates a dark exciton population is well established in van der Waals heterostructures [15].

IV. CONCLUSION

To summarize, we have systematically investigated the excitonic landscape in single-layer WSe_2/MoS_2 heterojunctions, focusing on the role of different stacking configurations. On the one hand, our analysis reveals that tightly bound excitons with an interlayer 3D character are uniquely present in the AA and AB_{Se} stackings, where the atomic registry enables strong out-of-plane hybridization via transition-metal d orbitals (Mo/W) coupling. On the other hand, 2D excitons and interlayer charge-transfer excitons can be found in all stacking types, showing that in-plane quantum confinement and interlayer dipole coupling are strong regardless of differences in symmetry. These findings highlight the delicate interplay between structural arrangement and excitonic properties, providing key tools for engineering van der Waals heterostructures with tailored electronic and optical responses.

The flat and commensurate stacking configurations examined in the present study occur within real materials, as observed in transition metal dichalcogenides (TMDs) and their vdW heterostructures [22,91–93]. As a consequence, our results offer important insights into the electronic and optical properties of such microscopic regions, which can significantly influence the behavior of the overall system. This is particularly relevant in the context of Moiré crystals, which are distinguished by their complex interlayer arrangements and rotational alignments, as reported in TMD-based vdW heterojunctions [22,22,91–107]. Our results contribute to a deeper understanding of fundamental structure-property relationships at the cutting edge of ab initio many-body theory, building on recent advances in the study of TMD-based vdW heterostructures and their emergent phenomena [95]. Despite the fact that these advanced computational methods are often challenging for modeling superlattices with realistic unit cell sizes due to their substantial computational demands, they provide us with essential basic data for constructing model Hamiltonians and semiempirical approaches capable of addressing these complex systems, as highlighted in recent studies on TMD-based vdW heterostructures [108–113]. These insights are crucial for advancing the design and understanding of next-generation quantum materials and devices based on TMD vdW heterostructures [33].

ACKNOWLEDGMENTS

This work has been supported by the open research fund of the General Direction of Research and Technological Development (DGRSDT) of the Ministry of Higher Education and Scientific Research, Algeria, and by the Deutsche Forschungsgemeinschaft (DFG, German Research Foundation) through the research unit QUAST, FOR 5249 P7 ID No. 449872909. *Ab initio* simulations were performed using computational resources from the HPC facility at the University of Batna 2 (Algeria), local clusters from CNR ISM at Monterotondo (Italy), and the Head1 ITP cluster at Heidelberg University (Germany) under the scholarship Coimbra 2024. M.P. acknowledges EOCOE III project. W.L. and K.R. thank Andrea Marini for his outstanding help and valuable advice, W.L. acknowledges Fulvio Paleari for technical assistance with the Yambo code and Yambopy toolkit.

DATA AVAILABILITY

The data that support the findings of this article are openly available [114].

[1] K. S. Novoselov, A. Mishchenko, A. Carvalho, and A. H. C. Neto, 2D materials and van der Waals heterostructures, Science **353**, aac9439 (2016).

[2] F. Xia, H. Wang, D. Xiao, M. Dubey, and A. Ramasubramaniam, Two-dimensional material nanophotonics, Nat. Photon. **8**, 899 (2014).

[3] H. Fang, S. Chuang, T. C. Chang, K. Takei, T. Takahashi, and A. Javey, High-performance single layered WSe_2 p-FETs with chemically doped contacts, Nano Lett. **12**, 3788 (2012).

[4] K. F. Mak, C. Lee, J. Hone, J. Shan, and T. F. Heinz, Atomically thin MoS_2: A new direct-gap semiconductor, Phys. Rev. Lett. **105**, 136805 (2010).

[5] K. F. Mak and J. Shan, Photonics and optoelectronics of 2D semiconductor transition metal dichalcogenides, Nat. Photon. **10**, 216 (2016).

[6] Q. H. Wang, K. Kalantar-Zadeh, A. Kis, J. N. Coleman, and M. S. Strano, Electronics and optoelectronics of two-dimensional transition metal dichalcogenides, Nat. Nanotechnol. **7**, 699 (2012).

[7] A. Splendiani, L. Sun, Y. Zhang, T. Li, J. Kim, C.-Y. Chim, G. Galli, and F. Wang, Emerging photoluminescence in monolayer MoS_2, Nano Lett. **10**, 1271 (2010).

[8] O. Lopez-Sanchez, D. Lembke, M. Kayci, A. Radenovic, and A. Kis, Ultrasensitive photodetectors based on monolayer MoS_2, Nat. Nanotechnol. **8**, 497 (2013).

[9] F. H. L. Koppens, T. Mueller, P. Avouris, A. C. Ferrari, M. S. Vitiello, and M. Polini, Photodetectors based on graphene, other two-dimensional materials and hybrid systems, Nat. Nanotechnol. **9**, 780 (2014).

[10] J. S. Ross, P. Klement, A. M. Jones, N. J. Ghimire, J. Yan, D. G. Mandrus, T. Taniguchi, K. Watanabe, K. Kitamura, W. Yao, D. H. Cobden, and X. Xu, Electrically tunable excitonic light-emitting diodes based on monolayer WSe_2 p–n junctions, Nat. Nanotechnol. **9**, 268 (2014).

[11] A. Pospischil, M. M. Furchi, and T. Mueller, Solar-energy conversion and light emission in an atomic monolayer p–n diode, Nat. Nanotechnol. **9**, 257 (2014).

[12] B. W. H. Baugher, H. O. H. Churchill, Y. Yang, and P. Jarillo-Herrero, Optoelectronic devices based on electrically tunable p–n diodes in a monolayer dichalcogenide, Nat. Nanotechnol. **9**, 262 (2014).

[13] M. Bernardi, M. Palummo, and J. C. Grossman, Extraordinary sunlight absorption and one nanometer thick photovoltaics using two-dimensional monolayer materials, Nano Lett. **13**, 3664 (2013).

[14] M. M. Furchi, A. Pospischil, F. Libisch, J. Burgdörfer, and T. Mueller, Photovoltaic effect in an electrically tunable van der Waals heterojunction, Nano Lett. **14**, 4785 (2014).

[15] G. Wang, A. Chernikov, M. M. Glazov, T. F. Heinz, X. Marie, T. Amand, and B. Urbaszek, Colloquium: Excitons in atomically thin transition metal dichalcogenides, Rev. Mod. Phys. **90**, 021001 (2018).

[16] T. Cao, G. Wang, W. Han, H. Ye, C. Zhu, J. Shi, Q. Niu, P. Tan, E. Wang, B. Liu, and J. Feng, Valley-selective circular dichroism of monolayer molybdenum disulphide, Nat. Commun. **3**, 887 (2012).

[17] X. Xu, W. Yao, D. Xiao, and T. F. Heinz, Spin and pseudospins in layered transition metal dichalcogenides, Nat. Phys. **10**, 343 (2014).

[18] D. Xiao, G.-B. Liu, W. Feng, X. Xu, and W. Yao, Coupled spin and valley physics in monolayers of MoS_2 and other group-VI dichalcogenides, Phys. Rev. Lett. **108**, 196802 (2012).

[19] K. F. Mak, K. L. McGill, J. Park, and P. L. McEuen, The valley Hall effect in MoS_2 transistors, Science **344**, 1489 (2014).

[20] A. Kormányos, G. Burkard, M. Gmitra, J. Fabian, V. Zólyomi, N. D. Drummond, and V. Fal'ko, k·p theory for two-dimensional transition metal dichalcogenide semiconductors, 2D Mater. **2**, 022001 (2015).

[21] A. K. Geim and I. V. Grigorieva, Van der Waals heterostructures, Nature (London) **499**, 419 (2013).

[22] C. Zhang, C.-P. Chuu, X. Ren, M.-Y. Li, L.-J. Li, C. Jin, M.-Y. Chou, and C.-K. Shih, Interlayer couplings, Moiré patterns, and 2D electronic superlattices in MoS_2/WSe_2 hetero-bilayers., Sci. Adv. **3**, e1601459 (2017).

[23] C.-H. Lee, G.-H. Lee, A. M. van der Zande, W. Chen, Y. Li, M. Han, X. Cui, G. Arefe, C. Nuckolls, T. F. Heinz, J. Guo, J. Hone, and P. Kim, Atomically thin p–n junctions with van der Waals heterointerfaces, Nat. Nanotechnol. **9**, 676 (2014).

[24] Y. Yu, Y. Yu, C. Xu, A. Barrette, K. Gundogdu, and L. Cao, Fundamental limits of exciton-exciton annihilation for light emission in transition metal dichalcogenide monolayers, Phys. Rev. B **93**, 201111 (2016).

[25] M. Palummo, M. Bernardi, and J. C. Grossman, Exciton radiative lifetimes in two-dimensional transition metal dichalcogenides, Nano Lett. **15**, 2794 (2015).

[26] A. Molina-Sánchez, D. Sangalli, K. Hummer, A. Marini, and L. Wirtz, Effect of spin-orbit interaction on the optical spectra of single-layer, double-layer, and bulk MoS_2, Phys. Rev. B **88**, 045412 (2013).

[27] Y. Gong, J. Lin, X. Wang, G. Shi, S. Lei, Z. Lin, X. Zou, G. Ye, R. Vajtai, B. I. Yakobson, H. Terrones, M. Terrones, B. Tay, J. Lou, S. T. Pantelides, Z. Liu, W. Zhou, and P. M. Ajayan, Vertical and in-plane heterostructures from WS_2/MoS_2 monolayers, Nat. Mater. **13**, 1135 (2014).

[28] L. Britnell, R. M. Ribeiro, A. Eckmann, R. Jalil, B. D. Belle, A. Mishchenko, Y.-J. Kim, R. V. Gorbachev, T. Georgiou, S. V. Morozov, A. N. Grigorenko, A. K. Geim, C. Casiraghi, A. H. C. Neto, and K. S. Novoselov, Strong light-matter interactions in heterostructures of atomically thin films, Science **340**, 1311 (2013).

[29] W. Aggoune, C. Cocchi, D. Nabok, K. Rezouali, M. Akli Belkhir, and C. Draxl, Enhanced light–matter interaction in graphene/h-BN van der Waals heterostructures, J. Phys. Chem. Lett. **8**, 1464 (2017).

[30] E. C. Regan, D. Wang, C. Jin, M. I. Bakti Utama, B. Gao, X. Wei, S. Zhao, W. Zhao, Z. Zhang, K. Yumigeta, M. Blei, J. D. Carlström, K. Watanabe, T. Taniguchi, S. Tongay, M. Crommie, A. Zettl, and F. Wang, Mott and generalized Wigner crystal states in WSe_2/WS_2 moiré superlattices, Nature (London) **579**, 359 (2020).

[31] Y. Tang, L. Li, T. Li, Y. Xu, S. Liu, K. Barmak, K. Watanabe, T. Taniguchi, A. H. MacDonald, J. Shan, and K. F. Mak, Simulation of Hubbard model physics in WSe_2/WS_2 moiré superlattices, Nature (London) **579**, 353 (2020).

[32] L. Britnell, R. V. Gorbachev, R. Jalil, B. D. Belle, F. Schedin, A. Mishchenko, T. Georgiou, M. I. Katsnelson, L. Eaves, S. V. Morozov, N. M. R. Peres, J. Leist, A. K. Geim, K. S. Novoselov, and L. A. Ponomarenko, Field-effect tunneling transistor based on vertical graphene heterostructures, Science **335**, 947 (2012).

[33] F. Withers, O. Del Pozo-Zamudio, A. Mishchenko, A. P. Rooney, A. Gholinia, K. Watanabe, T. Taniguchi, S. J. Haigh, A. K. Geim, A. I. Tartakovskii, and K. S. Novoselov, Light-emitting diodes by band-structure engineering in van der Waals heterostructures, Nat. Mater. **14**, 301 (2015).

[34] P. Hohenberg and W. Kohn, Inhomogeneous electron gas, Phys. Rev. **136**, B864 (1964).

[35] W. Kohn and L. J. Sham, Self-consistent equations including exchange and correlation effects, Phys. Rev. **140**, A1133 (1965).

[36] L. Hedin, New method for calculating the one-particle Green's function with application to the electron-gas problem, Phys. Rev. **139**, A796 (1965).

[37] M. S. Hybertsen and S. G. Louie, First-principles theory of quasiparticles: Calculation of band gaps in semiconductors and insulators, Phys. Rev. Lett. **55**, 1418 (1985).

[38] M. Rohlfing and S. G. Louie, Electron-hole excitations and optical spectra from first principles, Phys. Rev. B **62**, 4927 (2000).

[39] G. Onida, L. Reining, and A. Rubio, Electronic excitations: density-functional versus many-body Green's-function approaches, Rev. Mod. Phys. **74**, 601 (2002).

[40] W. Hanke and L. J. Sham, Many-particle effects in the optical spectrum of a semiconductor, Phys. Rev. B **21**, 4656 (1980).

[41] G. Strinati, Application of the Green's functions method to the study of the optical properties of semiconductors, Riv. Nuovo Cim. **11**, 1 (1988).

[42] P. Giannozzi, S. Baroni, N. Bonini, M. Calandra, R. Car, C. Cavazzoni, D. Ceresoli, G. L. Chiarotti, M. Cococcioni, I. Dabo *et al.*, QUANTUM ESPRESSO: a modular and open-source software project for quantum simulations of materials, J. Phys.: Condens. Matter **21**, 395502 (2009).

[43] A. Marini, C. Hogan, M. Grüning, and D. Varsano, yambo: An *ab initio* tool for excited state calculations, Comput. Phys. Commun. **180**, 1392 (2009).

[44] D. Sangalli, A. Ferretti, H. Miranda, C. Attaccalite, I. Marri, E. Cannuccia, P. Melo, M. Marsili, F. Paleari, A. Marrazzo, G. Prandini, P. Bonfà, M. O. Atambo, F. Affinito, M. Palummo, A. Molina-Sánchez, C. Hogan, M. Grüning, D. Varsano, and A. Marini, Many-body perturbation theory calculations using the yambo code, J. Phys.: Condens. Matter **31**, 325902 (2019).

[45] D. R. Hamann, Optimized norm-conserving Vanderbilt pseudopotentials, Phys. Rev. B **88**, 085117 (2013).

[46] J. P. Perdew, K. Burke, and M. Ernzerhof, Generalized gradient approximation made simple, Phys. Rev. Lett. **77**, 3865 (1996).

[47] S. Grimme, J. Antony, S. Ehrlich, and H. Krieg, A consistent and accurate *ab initio* parametrization of density functional dispersion correction (DFT-D) for the 94 elements H-Pu, J. Chem. Phys. **132**, 154104 (2010).

[48] T. Cheiwchanchamnangij and W. R. L. Lambrecht, Quasiparticle band structure calculation of monolayer, bilayer, and bulk MoS_2, Phys. Rev. B **85**, 205302 (2012).

[49] H. J. Monkhorst and J. D. Pack, Special points for Brillouin-zone integrations, Phys. Rev. B **13**, 5188 (1976).

[50] A. Guandalini, P. D'Amico, A. Ferretti, and D. Varsano, Efficient GW calculations in two dimensional materials through a stochastic integration of the screened potential, npj Comput. Mater. **9**, 44 (2023).

[51] R. W. Godby and R. J. Needs, Metal-insulator transition in Kohn-Sham theory and quasiparticle theory, Phys. Rev. Lett. **62**, 1169 (1989).

[52] See Supplemental Material at http://link.aps.org/supplemental/10.1103/n6py-mmq7 for additional results, including GW–BSE convergence tests, optical absorption spectra from the random-phase approximation (RPA) and BSE, exciton charge density distributions, and exciton weights projected onto the interpolated band structure.

[53] C. A. Rozzi, D. Varsano, A. Marini, E. K. U. Gross, and A. Rubio, Exact Coulomb cutoff technique for supercell calculations, Phys. Rev. B **73**, 205119 (2006).

[54] J. D. Bernal, The structure of graphite, Proc. R. Soc. Lond. A **106**, 749 (1924).

[55] G. Constantinescu, A. Kuc, and T. Heine, Stacking in bulk and bilayer hexagonal boron nitride, Phys. Rev. Lett. **111**, 036104 (2013).

[56] Y.-C. Lin, R. Ghosh, R. K. Ghosh, R. Addou, N. Lu, S. M. Eichfeld, H. Zhu, M.-Y. Li, X. Peng, M. J. Kim, L.-J. Li, R. M. Wallace, S. Datta, and J. A. Robinson, Atomically thin resonant tunnel diodes built from synthetic van der Waals heterostructures, Nat. Commun. **6**, 7311 (2015).

[57] Y. Ding, Y. Wang, J. Ni, L. Shi, S. Shi, and W. Tang, First principles study of structural, vibrational and electronic properties of graphene-like MX_2 (M=Mo, Nb, W, Ta; X=S, Se, Te) monolayers, Phys. B: Condens. Matter **406**, 2254 (2011).

[58] C.-H. Chang, X. Fan, S.-H. Lin, and J.-L. Kuo, Orbital analysis of electronic structure and phonon dispersion in MoS_2, $MoSe_2$, WS_2, and WSe_2 monolayers under strain, Phys. Rev. B **88**, 195420 (2013).

[59] A. Ramasubramaniam, Large excitonic effects in monolayers of molybdenum and tungsten dichalcogenides, Phys. Rev. B **86**, 115409 (2012).

[60] D. Le, A. Barinov, E. Preciado, M. Isarraraz, I. Tanabe, T. Komesu, C. Troha, L. Bartels, T. S. Rahman, and P. A. Dowben, Spin–orbit coupling in the band structure of monolayer WSe_2, J. Phys.: Condens. Matter **27**, 182201 (2015).

[61] G. J. Slotman, G. A. de Wijs, A. Fasolino, and M. I. Katsnelson, Phonons and electron-phonon coupling in graphene-*h*-BN heterostructures, Ann. Phys. (NY) **526**, 381 (2014).

[62] M. Milko, P. Puschnig, and C. Draxl, Predicting the electronic structure of weakly interacting hybrid systems: The example of nanosized peapod structures, Phys. Rev. B **86**, 155416 (2012).

[63] N. Dadkhah and W. R. L. Lambrecht, Band structure and excitonic properties of WSe_2 in the isolated monolayer limit in an all-electron approach, Phys. Rev. B **109**, 195155 (2024).

[64] D. Y. Qiu, F. H. da Jornada, and S. G. Louie, Optical spectrum of MoS_2: Many-body effects and diversity of exciton states, Phys. Rev. Lett. **111**, 216805 (2013).

[65] K. Dange, R. Yogi, and A. Shukla, Two-dimensional transition-metal dichalcogenide–based bilayer heterojunctions for efficient solar cells and photocatalytic applications, Phys. Rev. Appl. **23**, 014008 (2025).

[66] H. Terrones, F. López-Urías, and M. Terrones, Novel hetero-layered materials with tunable direct band gaps by sandwiching different metal disulfides and diselenides, Sci. Rep. **3**, 1549 (2013).

[67] Y.-C. Shih, F. A. Nilsson, and G.-Y. Guo, Electron energy loss spectra and exciton band structure of WSe_2 monolayers studied by *ab initio* Bethe-Salpeter equation calculations, Phys. Rev. B **110**, 205417 (2024).

[68] E. S. Kadantsev and P. Hawrylak, Electronic structure of a single MoS_2 monolayer, Solid State Commun. **152**, 909 (2012).

[69] M. Feierabend, A. Morlet, G. Berghäuser, and E. Malic, Impact of strain on the optical fingerprint of monolayer transition-metal dichalcogenides, Phys. Rev. B **96**, 045425 (2017).

[70] A. M. Kumar, D. Yagodkin, R. Rosati, D. J. Bock, C. Schattauer, S. Tobisch, J. Hagel, B. Höfer, J. N. Kirchhof, P. Hernández López, K. Burfeindt, S. Heeg, C. Gahl, F. Libisch, E. Malic, and K. I. Bolotin, Strain fingerprinting of exciton

valley character in 2D semiconductors, Nat. Commun. **15**, 7546 (2024).

[71] B. Aslan, M. Deng, and T. F. Heinz, Strain tuning of excitons in monolayer WSe_2, Phys. Rev. B **98**, 115308 (2018).

[72] F. Carrascoso, D.-Y. Lin, R. Frisenda, and A. Castellanos-Gomez, Biaxial strain tuning of interlayer excitons in bilayer MoS_2, J. Phys.: Mater. **3**, 015003 (2019).

[73] E. Blundo, E. Cappelluti, M. Felici, G. Pettinari, and A. Polimeni, Strain-tuning of the electronic, optical, and vibrational properties of two-dimensional crystals, Appl. Phys. Rev. **8**, 021318 (2021).

[74] M. Marsili, A. Molina-Sánchez, M. Palummo, D. Sangalli, and A. Marini, Spinorial formulation of the GW-BSE equations and spin properties of excitons in two-dimensional transition metal dichalcogenides, Phys. Rev. B **103**, 155152 (2021).

[75] R. Schmidt, I. Niehues, R. Schneider, M. Drüppel, T. Deilmann, M. Rohlfing, S. M. de Vasconcellos, A. Castellanos-Gomez, and R. Bratschitsch, Reversible uniaxial strain tuning in atomically thin WSe_2, 2D Mater. **3**, 021011 (2016).

[76] W. Aggoune, C. Cocchi, D. Nabok, K. Rezouali, M. A. Belkhir, and C. Draxl, Dimensionality of excitons in stacked van der Waals materials: The example of hexagonal boron nitride, Phys. Rev. B **97**, 241114 (2018).

[77] P. Rivera, J. R. Schaibley, A. M. Jones, J. S. Ross, S. Wu, G. Aivazian, P. Klement, K. Seyler, G. Clark, N. J. Ghimire, J. Yan, D. G. Mandrus, W. Yao, and X. Xu, Observation of long-lived interlayer excitons in monolayer $MoSe_2$–WSe_2 heterostructures, Nat. Commun. **6**, 6242 (2015).

[78] D. Huang, J. Choi, C.-K. Shih, and X. Li, Excitons in semiconductor moiré superlattices, Nat. Nanotechnol. **17**, 227 (2022).

[79] C. Deibel, T. Strobel, and V. Dyakonov, Role of the charge transfer state in organic donor–acceptor solar cells, Adv. Mater. **22**, 4097 (2010).

[80] T. M. Clarke and J. R. Durrant, Charge photogeneration in organic solar cells, Chem. Rev. **110**, 6736 (2010).

[81] F. Cadiz, E. Courtade, C. Robert, G. Wang, Y. Shen, H. Cai, T. Taniguchi, K. Watanabe, H. Carrere, D. Lagarde, M. Manca, T. Amand, P. Renucci, S. Tongay, X. Marie, and B. Urbaszek, Excitonic linewidth approaching the homogeneous limit in MoS_2-based van der Waals heterostructures, Phys. Rev. X **7**, 021026 (2017).

[82] C. Robert, D. Lagarde, F. Cadiz, G. Wang, B. Lassagne, T. Amand, A. Balocchi, P. Renucci, S. Tongay, B. Urbaszek, and X. Marie, Exciton radiative lifetime in transition metal dichalcogenide monolayers, Phys. Rev. B **93**, 205423 (2016).

[83] J. Huang, T. B. Hoang, and M. H. Mikkelsen, Probing the origin of excitonic states in monolayer WSe_2, Sci. Rep. **6**, 22414 (2016).

[84] B. Miller, A. Steinhoff, B. Pano, J. Klein, F. Jahnke, A. Holleitner, and U. Wurstbauer, Long-lived direct and indirect interlayer excitons in van der Waals heterostructures, Nano Lett. **17**, 5229 (2017).

[85] A. A. Bakulin, A. Rao, V. G. Pavelyev, P. H. M. van Loosdrecht, M. S. Pshenichnikov, D. Niedzialek, J. Cornil, D. Beljonne, and R. H. Friend, The role of driving energy and delocalized states for charge separation in organic semiconductors, Science **335**, 1340 (2012).

[86] L. A. Jauregui, A. Y. Joe, K. Pistunova, D. S. Wild, A. A. High, Y. Zhou, G. Scuri, K. De Greve, A. Sushko, C.-H. Yu, T. Taniguchi, K. Watanabe, D. J. Needleman, M. D. Lukin, H. Park, and P. Kim, Electrical control of interlayer exciton dynamics in atomically thin heterostructures, Science **366**, 870 (2019).

[87] S. Gélinas, A. Rao, A. Kumar, S. L. Smith, A. W. Chin, J. Clark, T. S. van der Poll, G. C. Bazan, and R. H. Friend, Ultrafast long-range charge separation in organic semiconductor photovoltaic diodes, Science **343**, 512 (2014).

[88] A. Chernikov, A. M. van der Zande, H. M. Hill, A. F. Rigosi, A. Velauthapillai, J. Hone, and T. F. Heinz, Electrical tuning of exciton binding energies in monolayer WS_2, Phys. Rev. Lett. **115**, 126802 (2015).

[89] N. Leisgang, S. Shree, I. Paradisanos, L. Sponfeldner, C. Robert, D. Lagarde, A. Balocchi, K. Watanabe, T. Taniguchi, X. Marie, R. J. Warburton, I. C. Gerber, and B. Urbaszek, Giant Stark splitting of an exciton in bilayer MoS_2, Nat. Nanotechnol. **15**, 901 (2020).

[90] X. Hong, J. Kim, S.-F. Shi, Y. Zhang, C. Jin, Y. Sun, S. Tongay, J. Wu, Y. Zhang, and F. Wang, Ultrafast charge transfer in atomically thin MoS_2/WS_2 heterostructures, Nat. Nanotechnol. **9**, 682 (2014).

[91] J. H. Yu, H. R. Lee, S. S. Hong, D. Kong, H.-W. Lee, H. Wang, F. Xiong, S. Wang, and Y. Cui, Vertical heterostructure of two-dimensional MoS_2 and WSe_2 with vertically aligned layers, Nano Lett. **15**, 1031 (2015).

[92] E. M. Alexeev, D. A. Ruiz-Tijerina, M. Danovich, M. J. Hamer, D. J. Terry, P. K. Nayak, S. Ahn, S. Pak, J. Lee, J. I. Sohn, M. R. Molas, M. Koperski, K. Watanabe, T. Taniguchi, K. S. Novoselov, R. V. Gorbachev, H. S. Shin, V. I. Fal'ko, and A. I. Tartakovskii, Resonantly hybridized excitons in moiré superlattices in van der Waals heterostructures, Nature (London) **567**, 81 (2019).

[93] E. M. Alexeev, C. M. Purser, C. M. Gilardoni, J. Kerfoot, H. Chen, A. R. Cadore, B. L. Rosa, M. S. G. Feuer, E. Javary, P. Hays, K. Watanabe, T. Taniguchi, S. A. Tongay, D. M. Kara, M. Atatüre, and A. C. Ferrari, Nature of long-lived Moiré interlayer excitons in electrically tunable MoS_2/$MoSe_2$ heterobilayers, Nano Lett. **24**, 11232 (2024).

[94] E. M. Alexeev, A. Catanzaro, O. V. Skrypka, P. K. Nayak, S. Ahn, S. Pak, J. Lee, J. I. Sohn, K. S. Novoselov, H. S. Shin, and A. I. Tartakovskii, Imaging of interlayer coupling in van der Waals heterostructures using a bright-field optical microscope, Nano Lett. **17**, 5342 (2017).

[95] P. Merkl, F. Mooshammer, P. Steinleitner, A. Girnghuber, K.-Q. Lin, P. Nagler, J. Holler, C. Schüller, J. M. Lupton, T. Korn, S. Ovesen, S. Brem, E. Malic, and R. Huber, Ultrafast transition between exciton phases in van der Waals heterostructures, Nat. Mater. **18**, 691 (2019).

[96] T. Deilmann and K. S. Thygesen, Interlayer excitons with large optical amplitudes in layered van der Waals materials, Nano Letters **18**, 2984 (2018).

[97] C. Gong, H. Zhang, W. Wang, L. Colombo, R. M. Wallace, and K. Cho, Band alignment of two-dimensional transition metal dichalcogenides: Application in tunnel field effect transistors, Appl. Phys. Lett. **103**, 053513 (2013).

[98] J. Kang, S. Tongay, J. Zhou, J. Li, and J. Wu, Band offsets and heterostructures of two-dimensional semiconductors, Appl. Phys. Lett. **102**, 012111 (2013).

[99] Y. Wang, Z. Wang, W. Yao, G.-B. Liu, and H. Yu, Interlayer coupling in commensurate and incommensurate bilayer struc-

tures of transition-metal dichalcogenides, Phys. Rev. B **95**, 115429 (2017).

[100] D. Kozawa, A. Carvalho, I. Verzhbitskiy, F. Giustiniano, Y. Miyauchi, S. Mouri, A. H. Castro Neto, K. Matsuda, and G. Eda, Evidence for fast interlayer energy transfer in $MoSe_2/WS_2$ heterostructures, Nano Lett. **16**, 4087 (2016).

[101] K. L. Seyler, P. Rivera, H. Yu, N. P. Wilson, E. L. Ray, D. G. Mandrus, J. Yan, W. Yao, and X. Xu, Signatures of moiré-trapped valley excitons in $MoSe_2/WSe_2$ heterobilayers, Nature (London) **567**, 66 (2019).

[102] K. Tran, G. Moody, F. Wu, X. Lu, J. Choi, K. Kim, A. Rai, D. A. Sanchez, J. Quan, A. Singh, J. Embley, A. Zepeda, M. Campbell, T. Autry, T. Taniguchi, K. Watanabe, N. Lu, S. K. Banerjee, K. L. Silverman, S. Kim, E. Tutuc, L. Yang, A. H. MacDonald, and X. Li, Evidence for moiré excitons in van der Waals heterostructures, Nature (London) **567**, 71 (2019).

[103] J. Kunstmann, F. Mooshammer, P. Nagler, A. Chaves, F. Stein, N. Paradiso, G. Plechinger, C. Strunk, C. Schüller, G. Seifert, D. R. Reichman, and T. Korn, Momentum-space indirect interlayer excitons in transition-metal dichalcogenide van der Waals heterostructures, Nat. Phys. **14**, 801 (2018).

[104] P. K. Nayak, Y. Horbatenko, S. Ahn, G. Kim, J.-U. Lee, K. Y. Ma, A.-R. Jang, H. Lim, D. Kim, S. Ryu, H. Cheong, N. Park, and H. S. Shin, Probing evolution of twist-angle-dependent interlayer excitons in $MoSe_2/WSe_2$ van der Waals heterostructures, ACS Nano **11**, 4041 (2017).

[105] H. Heo, J. H. Sung, S. Cha, B.-G. Jang, J.-Y. Kim, G. Jin, D. Lee, J.-H. Ahn, M.-J. Lee, J. H. Shim, H. Choi, and M.-H. Jo, Interlayer orientation-dependent light absorption and emission in monolayer semiconductor stacks, Nat. Commun. **6**, 7372 (2015).

[106] F. Wu, T. Lovorn, and A. H. MacDonald, Topological exciton bands in Moiré heterojunctions, Phys. Rev. Lett. **118**, 147401 (2017).

[107] A. M. van der Zande, J. Kunstmann, A. Chernikov, D. A. Chenet, Y. You, X. Zhang, P. Y. Huang, T. C. Berkelbach, L. Wang, F. Zhang, M. S. Hybertsen, D. A. Muller, D. R. Reichman, T. F. Heinz, and J. C. Hone, Tailoring the electronic structure in bilayer molybdenum disulfide via interlayer twist, Nano Lett. **14**, 3869 (2014).

[108] P. Tscheppe, J. Zang, M. Klett, S. Karakuzu, A. Celarier, Z. Cheng, C. A. Marianetti, T. A. Maier, M. Ferrero, A. J. Millis, and T. Schäfer, Magnetism and metallicity in moiré transition metal dichalcogenides, Proc. Natl. Acad. Sci. USA **121**, e2311486121 (2024).

[109] M. Förg, A. S. Baimuratov, S. Y. Kruchinin, I. A. Vovk, J. Scherzer, J. Förste, V. Funk, K. Watanabe, T. Taniguchi, and A. Högele, Moiré excitons in $MoSe_2 - WSe_2$ heterobilayers and heterotrilayers, Nat. Commun. **12**, 1656 (2021).

[110] V. Crépel and A. Millis, Bridging the small and large in twisted transition metal dichalcogenide homobilayers: A tight binding model capturing orbital interference and topology across a wide range of twist angles, Phys. Rev. Res. **6**, 033127 (2024).

[111] T. Rakib, P. Pochet, E. Ertekin, and H. T. Johnson, Moiré engineering in van der Waals heterostructures, J. Appl. Phys. **132**, 120901 (2022).

[112] T. Devakul, V. Crépel, Y. Zhang, and L. Fu, Magic in twisted transition metal dichalcogenide bilayers, Nat. Commun. **12**, 6730 (2021).

[113] A. Ramos-Alonso, B. Remez, D. Bennett, R. M. Fernandes, and H. Ochoa, Flat and tunable Moiré phonons in twisted transition-metal dichalcogenides, Phys. Rev. Lett. **134**, 026501 (2025).

[114] https://nomad-lab.eu/prod/v1/gui/user/datasets/dataset/id/Uk9TGquxQ9qnofy74xpS6A.